Robust quantum control using hybrid pulse engineering

M. Harshanth Ram,* V. R. Krithika,† Priya Batra,‡ and T. S. Mahesh§
Department of Physics and NMR Research Center, Indian Institute of Science Education and Research, Pune 411008, India

(Received 20 December 2021; accepted 29 March 2022; published 28 April 2022)

The development of efficient algorithms that generate robust quantum controls is crucial for the realization of quantum technologies. The commonly used gradient-based optimization algorithms are limited by their sensitivity to the initial guess, which affects their performance. Here we propose combining the gradient method with the simulated annealing technique to formulate a hybrid algorithm. Our numerical analysis confirms its superior convergence rate. Using the hybrid algorithm, we generate spin-selective π pulses and employ them for experimental measurement of local noise spectra in a three-qubit nuclear magnetic resonance system. Moreover, here we describe a general method to construct noise-resilient quantum controls by incorporating noisy fields within the optimization routine of the hybrid algorithm. Upon experimental comparison with similar sequences obtained from standard algorithms, we find remarkable robustness of the hybrid sequences against dephasing errors.

DOI: 10.1103/PhysRevA.105.042437

I. INTRODUCTION

Driven by quantum technology goals, the control of quantum mechanical systems has become an important topic of research in recent years. Robust quantum control lies at the cornerstone of any efficient and reliable quantum processor. The building blocks of a quantum processor, the qubits, must be precisely controlled and protected against systematic deviations in the control fields, as well as against the random noise-induced by the surrounding environment. Accordingly, a plethora of control techniques have been developed, which include gradient-based approaches such as strongly modulated pulses [1,2], gradient ascent pulse engineering (GRAPE) [3,4], gradient optimization of analytical control [5], truncated basis approaches such as chopped random basis optimization [6,7], variational-principle-based techniques like relaxation optimized pulse engineering [8], Krotov optimization [9–11], a combination of gradient and variational controls like the K-BFGS algorithm [12], evolutionary algorithm-based controls [13,14], and neural network and reinforcement learning inspired approaches [15,16].

Quantum control techniques have been realized in nuclear magnetic resonance (NMR) [17–20], nitrogen-vacancy centers [21], superconducting qubits [22], ion traps [23], magnetic resonance imaging [24], cold atoms [25], etc. Here we use NMR systems as a quantum platform to develop robust quantum control techniques. The availability of long-lasting spin coherences and highly adaptable control fields make NMR an ideal test bed for quantum control developments [26,27].

Generally, quantum control techniques are limited by two challenges: (i) sensitivity to the initial guess as well as local optima which limit the convergence efficiency of the optimization algorithms, and (ii) susceptibility to losing fidelity due to incoherence, decoherence, or a combination of both. In this article, we propose methodologies to combat both of these limitations (see Fig. 1). First, we propose combining GRAPE and simulated annealing (SA) [28,29] to realize a hybrid optimization technique called simulated annealing gradient ascent pulse engineering (SAGRAPE) that can overcome local optima and converge faster toward better solutions. Second, we propose optimizing SAGRAPE sequences along with certain random fields, yielding a robust algorithm, namely, robust simulated annealing gradient ascent pulse engineering (RSAGRAPE). It can generate control sequences that are resilient against environmental noises. Additionally, we describe integrating these sequences with standard dynamical decoupling sequences such as Carr-Purcell-Meiboom-Gill (CPMG) [30,31], which enhances their robustness. We numerically analyze the convergence efficiency and experimentally demonstrate the robustness of the hybrid sequences.

This article is organized as follows. In Sec. II, we describe the quantum system and revisit the GRAPE algorithm. Subsequently, we introduce the hybrid algorithm SAGRAPE and analyze its convergence efficiency. We then describe the NMR implementation of SAGRAPE sequences. In Sec. III we describe the SAGRAPE optimization in the presence of a random field to obtain RSAGRAPE, and we experimentally demonstrate the robustness of the RSAGRAPE sequence. Finally, we present the summary and the outlook in Sec. IV.

II. GRAPE AND SAGRAPE

In this section, we first describe the quantum system in which we are interested in establishing quantum control, in terms of both state-to-state transfer and realizing general

*m.harshanthram@students.iiserpune.ac.in
†krithika_vr@students.iiserpune.ac.in
‡priya.batra@students.iiserpune.ac.in
§mahesh.ts@iiserpune.ac.in

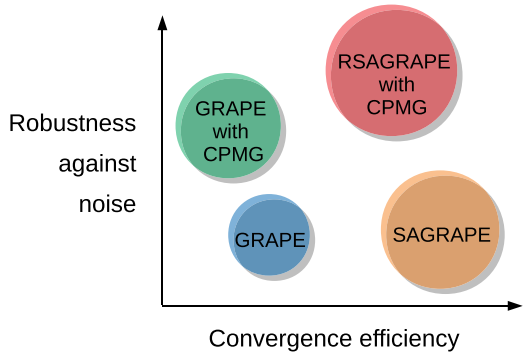

FIG. 1. Comparison of quantum control algorithms with respect to convergence efficiency and robustness against noise.

quantum gates. After reviewing the GRAPE and the SA algorithms, we explain the hybrid algorithm SAGRAPE and analyze its convergence efficiency. Finally, we describe an NMR application of SAGRAPE sequences.

A. The quantum system

We consider an n-qubit NMR system with a total rotating-frame (RF) Hamiltonian,

$$H(t) = H_0 + H_{\rm RF}(t), \quad \text{where}$$
$$H_0 = -\sum_k \Omega_k I_{kz} + 2\pi \sum_{kl} J_{kl} \mathbf{I}_k \cdot \mathbf{I}_l, \tag{1}$$

where Ω_k is the resonance offset, J_{kl} is the indirect spin-spin coupling constant, and $I_{k\alpha}$ with $\alpha \in \{x, y, z\}$ are components of the kth spin operator $\mathbf{I}_k$. Generally, we discretize the entire sequence of duration T into N equal segments each of duration $\tau = T/N$. We assume that the n spin qubits belong to s different species (isotopes) and the qth species is controllable with an RF sequence $\{\omega_{q\alpha}(j)\}$. The RF Hamiltonian for the jth segment is of the form

$$H_{\rm RF}(j) = \sum_{q=1}^{s} \sum_{\alpha=x,y} \omega_{q\alpha}(j) H_{q\alpha},$$
$$\text{with} \quad H_{q\alpha} = \sum_{k\in\{\text{species } q\}} I_{k\alpha}. \tag{2}$$

In this work, we consider only one type of nuclear species, i.e., $q = 1$, and hence we drop the subscript q from now onward.

In practice, there exists a spatial inhomogeneity of RF amplitudes which are modeled by a scaling factor r_m with an associated probability p_m. Thus for the mth subensemble, the total Hamiltonian of the jth segment is

$$H^m(j) = H_0 + H^m_{\rm RF}(j), \quad \text{with}$$
$$H^m_{\rm RF}(j) = r_m\{\omega_x(j)H_x + \omega_y(j)H_y\}. \tag{3}$$

The propagator for the entire sequence is written as

$$U^m = U^m_N U^m_{N-1} \cdots U^m_2 U^m_1, \quad \text{where} \tag{4}$$
$$U^m_j = \exp[-\iota\tau H^m(j)]$$

are the segment propagators. The control algorithms aim to generate the sequence $\{\omega_x(j), \omega_y(j)\}$ that performs a given quantum control task. In the following, we revisit the GRAPE algorithm that is commonly used for this purpose.

B. Gradient ascent pulse engineering (GRAPE)

Given a target operation, GRAPE starts with a random sequence $\{\omega^0_x(j), \omega^0_y(j)\}$, which is updated based on the local gradients. In our work, we consider the GRAPE algorithm whose gradients are correct up to the first order. Generally, we consider the following two types of quantum control.

1. State control

The objective here is to find a sequence that transforms an initial state ρ_0 into a target state ρ_F by finding a sequence that maximizes the average state fidelity:

$$\Phi = \sum_m p_m \langle \rho_F | U^m \rho_0 U^{m\dagger} \rangle = \sum_m p_m {\rm Tr}[\rho_F U^m \rho_0 U^{m\dagger}], \tag{5}$$

where the summation is carried out on the subensembles corresponding to RF inhomogeneity (RFI). The update rule for the ith iteration is [3]

$$\omega^{i+1}_\alpha(j) = \omega^i_\alpha(j) + \epsilon G^i_\alpha(j), \quad \text{where the gradient}$$
$$G^i_\alpha(j) = -\iota\tau \sum_m p_m \langle \lambda^{mi}_j | [H_\alpha, \rho^{mi}_j] \rangle, \quad \text{with}$$
$$\rho^{mi}_j = U^{mi}_j \cdots U^{mi}_1 \, \rho_0 U^{mi\dagger}_1 \cdots U^{mi\dagger}_j \quad \text{and}$$
$$\lambda^{mi}_j = U^{mi\dagger}_{j+1} \cdots U^{mi\dagger}_N \, \rho_F U^{mi}_N \cdots U^{mi}_{j+1} \tag{6}$$

being the forward and backward propagated states, respectively, and ϵ being the step size. The iterations are continued until the fidelity Φ reaches the desired value.

2. Gate control

Here the objective is to generate a sequence that realizes the desired propagator U_F by maximizing the gate fidelity:

$$\Phi = \sum_m p_m |\langle U | U_F \rangle|^2 = \sum_m p_m |{\rm Tr}[U^\dagger U_F]|^2. \tag{7}$$

The update rule for the ith iteration is [3]

$$\omega^{i+1}_\alpha(j) = \omega^i_\alpha(j) + \epsilon G^i_\alpha(j), \quad \text{where the gradient}$$
$$G^i_\alpha(j) = -2\iota\tau \sum_m p_m {\rm Re}\{\langle P^{mi}_j | H_\alpha X^{mi}_j \rangle \langle X^{mi}_j | P^{mi}_j \rangle\},$$
$$\text{with } X^{mi}_j = U^{mi}_j \, U^{mi}_{j-1} \cdots U^{mi}_2 \, U^{mi}_1 \text{ and}$$
$$P^{mi}_j = U^{mi\dagger}_{j+1} \, U^{mi\dagger}_{j+2} \cdots U^{mi\dagger}_{N-1} \, U^{mi\dagger}_N \, U_F \tag{8}$$

being the forward and backward propagators. Again, the iterations are continued until the fidelity Φ reaches the desired value.

C. Simulated annealing (SA)

SA is a single candidate-based metaheuristic algorithm that is used to reach the neighborhood of the global optimum of optimization function. Generally, one uses either a probabilistic-based selection [28] or a threshold-based selection [29,32]. In our work, we use the latter as explained in the following. The general idea of SA can be described as

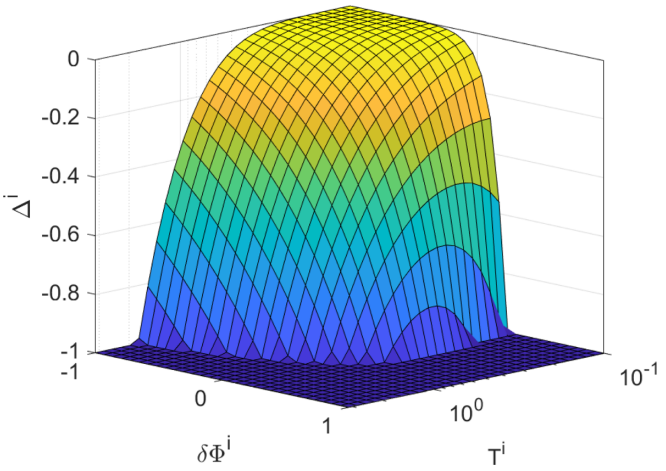

FIG. 2. Threshold-based acceptance function (Δ^i) plotted versus temperature T^i and the fidelity variation $\delta\Phi^i$. Note that Δ^i is bounded by $[-1, 0]$.

two modes—an exploration mode and an exploitation mode. In every iteration, a solution $\{\omega'_\alpha\}$ of fidelity $\Phi(\{\omega'_\alpha\})$ is randomly selected from the search space in the neighborhood of the current solution $\{\omega^i_\alpha\}$ with fidelity $\Phi(\{\omega^i_\alpha\})$. The current solution is replaced with the random solution if the fidelity variation is above a certain threshold function Δ^i such that

$$\delta\Phi^i = \Phi(\{\omega'_\alpha\}) - \Phi(\{\omega^i_\alpha\}) \geqslant \Delta^i. \tag{9}$$

In our work, we define the threshold function Δ^i as follows:

$$\Delta^i = -\min\left[1, T^i \exp\left(\frac{\delta\Phi^i}{T^i}\right)\right]. \tag{10}$$

Here T^i is referred to as the temperature of the current iteration in analogy to the thermodynamical processes. If $\delta\Phi^i \geqslant 0$, then the fidelity has improved with the random solution, and naturally $\{\omega^{i+1}_\alpha\}$ is set to $\{\omega'_\alpha\}$. However, notice that even if $\delta\Phi^i < 0$, i.e., the random solution is worse than the current solution, then we may still set $\{\omega^{i+1}_\alpha\}$ to $\{\omega'_\alpha\}$ as long as the threshold condition Eq. (9) is satisfied. Thus the algorithm is in an exploration mode, where it looks for a neighborhood with favorable solutions. This is the salient feature of the simulated annealing algorithm that enables it to get over the local optima. As explained above, the temperature parameter controls the threshold function for selecting nonoptimal solutions for subsequent iterations. The higher the temperature is, the greater are the chances for the random solution to lie within the threshold and become the next solution. However, as the algorithm approaches the global optimum, it should promote only candidates that increase the fidelity. Thus, in the initial iterations of SA, the temperature is kept high, and as iterations pass, the temperature is gradually reduced, thereby increasingly restricting nonoptimal solutions from passing through. Accordingly, the algorithm gradually shifts from exploration mode to exploitation mode. This is illustrated in Fig. 2, wherein the threshold function is plotted versus $\delta\Phi^i$ as well as temperature T^i.

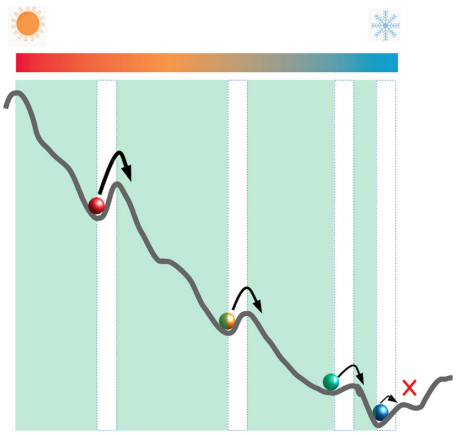

FIG. 3. Illustrating the progress of the SAGRAPE algorithm in bumpy parameter space. The green and white backgrounds respectively depict the regions where GRAPE and SA contribute toward minimization. GRAPE relies on monotonic convergence, while SA allows jumping over local maxima. As the algorithm proceeds, the temperature parameter of SA is gradually reduced to keep the solution trapped in the global minimum by restraining any further jumps.

D. SAGRAPE algorithm

Even though SA is efficient in getting out of the local optima and identifying a good neighborhood, it takes many iterations to get to the global optimum. On the other hand, a gradient-based algorithm like GRAPE [3] is much faster in identifying the best solution once a good neighborhood is reached. Thus, here we now introduce a hybrid algorithm of both SA and GRAPE (see Fig. 3). This way we can incorporate the best of both optimization techniques.

The flowchart for the SAGRAPE algorithm is shown in Fig. 4. We carry out κ iterations of SA before each GRAPE iteration to create one iteration of the SAGRAPE-κ algorithm. In every iteration i of SA, we need to generate a random solution and compare it with the threshold criterion of Eq. (9). In our implementation, we generate a set of 20 random solutions, each of which is obtained by perturbing the current solution $\{\omega^i_\alpha\}$ with a random spline function ω_s, i.e., $\omega^i_\alpha + \varepsilon^j\omega_s$, where ε^j is the step size that determines the size of the neighborhood. We reduce ε^j with the SAGRAPE iteration number j to gradually shrink the neighborhood size. Now we select the random solution $\{\omega'_\alpha\}$ with the highest fidelity $\Phi(\{\omega'_\alpha\})$ and compare it with the threshold criterion of Eq. (9). In each SAGRAPE iteration, the temperature parameter T is initially set to 0.5 (i.e., $T^0 = 0.5$) and then gradually reduced to move from exploration mode to exploitation mode. This is achieved by defining

$$T^{i+1} = \gamma^j T^i, \quad \text{where} \gamma^j = \left[\frac{1 - \Phi(\{\omega^G_\alpha\})}{2}\right]^{1/\kappa} \tag{11}$$

is the cooling factor, and $\{\omega^G_\alpha\}$ is the final solution of the $(j-1)$th SAGRAPE iteration.

The solution from the GRAPE algorithm of the current SAGRAPE iteration is chosen as the initial solution for the SA algorithm of the next SAGRAPE iteration (see Fig. 3).

Another possible benefit often observed in the hybrid algorithm is the following. The first-order approximation

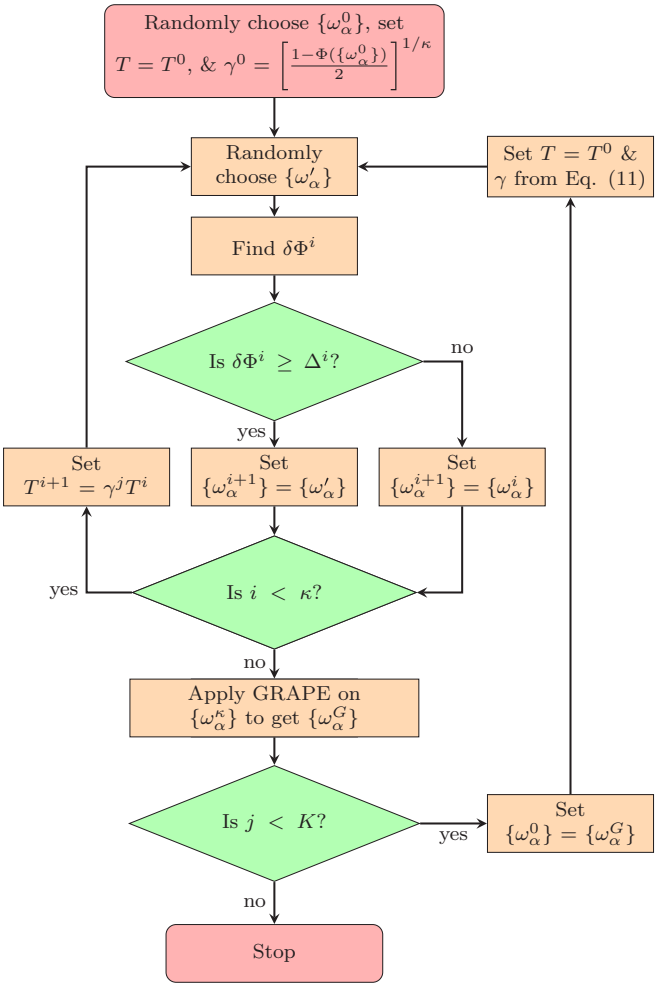

FIG. 4. Flowchart for the SAGRAPE algorithm. Here $i \leqslant \kappa$ and $j \leqslant K$ indicate iterations over SA and SAGRAPE, respectively.

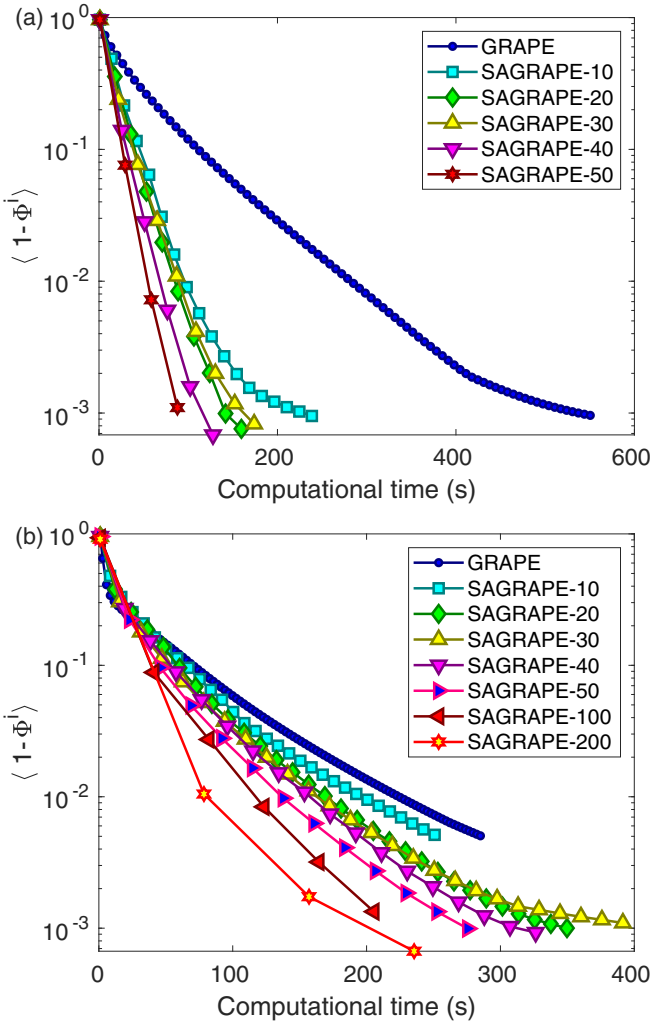

FIG. 5. Average infidelity $\langle 1 - \Phi^i \rangle$ in the ith iteration of SAGRAPE versus computational time taken by GRAPE and SAGRAPE-κ algorithms for (a) state control (preparing pseudo-singlet-triplet order) and (b) gate control (preparing CNOT gate) respectively. Each SAGRAPE-κ data point corresponds to κ number of SA iterations followed by one GRAPE iteration. Here each curve is obtained by averaging over five different trials starting from the random initial guess $\{\omega_\alpha^0(j)\}$. In each trial, the initial guess was kept the same across all the different cases.

$(|\Omega_k \tau| \leqslant 1 \; \forall \; k \in \{\text{species q}\})$ used in the GRAPE algorithm limits the maximum length of the time duration (τ) of the control sequence. Hence, for generating pulses with long time durations, it becomes necessary to use a large number of time steps (N), which increases the computation time. The SAGRAPE algorithm is resilient against this constraint to a certain extent due to the inclusion of SA which randomly selects a candidate based on the threshold function (Δ^i) without relying on the first-order approximation.

E. Convergence analysis of SAGRAPE

We now demonstrate the convergence of the SAGRAPE algorithm for state control and gate control in a two-qubit system. As an example, we consider a homonuclear two-spin system with resonance offsets $\Omega_{1(2)}/(2\pi) = \pm 63.7$ Hz and an indirect spin-spin coupling constant $J_{12} = 8.8$ Hz (corresponding to an experimental system described in Sec. III).

For state control, we generate the RF sequence $\{\omega_\alpha(j)\}$ that transforms the two-spin NMR thermal equilibrium state to the pseudo-singlet-triplet order, i.e.,

$$I_{z1} + I_{z2} \xrightarrow{\{\omega_\alpha(j)\}} -(\mathbf{I}_1^+\mathbf{I}_2^- + \mathbf{I}_1^-\mathbf{I}_2^+) = |S_0\rangle\langle S_0| - |T_0\rangle\langle T_0|, \quad (12)$$

where $S_0 = (|01\rangle - |10\rangle)/\sqrt{2}$ and $T_0 = (|01\rangle + |10\rangle)/\sqrt{2}$ are the singlet and triplet components, respectively. Similarly, for the gate control, we generate the sequence realizing the CNOT gate,

$$U = |0\rangle\langle 0| \otimes \mathbb{1} + |1\rangle\langle 1| \otimes \sigma_x, \quad (13)$$

where σ_x is the Pauli x operator which applies the NOT gate on the second qubit only if the first qubit is in state $|1\rangle$.

All the sequences prepared with the GRAPE and SAGRAPE algorithms have the same time duration of 120 ms discretized into 600 equal-duration segments. We carried out the convergence analysis of "SAGRAPE-κ" with varying numbers of SA iterations (κ) and compared the computational time with the GRAPE algorithm. The numerical results are shown in Fig. 5. Here Fig. 5(a) corresponds to the state

(a)

1F	2F	3F
6235.9	301.6	126.5
	-3298.5	-38.75
		-6375.3

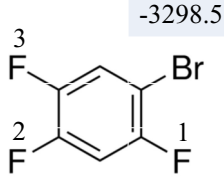

(b)

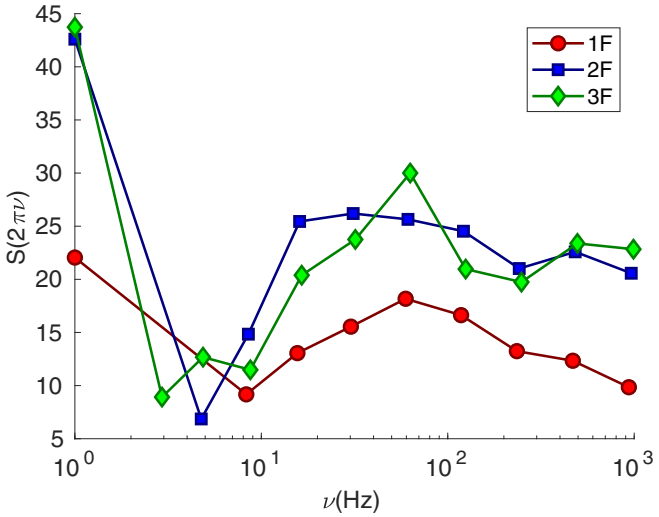

FIG. 6. (a) Molecular structure of BTFBz showing three ^{19}F nuclei and the table of resonance offsets $\Omega_k/(2\pi)$ (diagonal elements) and indirect spin-spin coupling constants J_{kl} (off-diagonal elements) in Hz. (b) Experimentally obtained local noise spectrum for each ^{19}F spin.

control, where we prepare the pseudo-singlet-triplet order, wherein we see a significant improvement of convergence by the hybrid algorithm. Figure 5(b) corresponds to the gate control, wherein we observed an improvement, but not as pronounced as in the state control. It is evident that SA significantly improves the convergence efficiency in both state and gate control tasks.

F. NMR demonstration of SAGRAPE

Now we demonstrate an experimental utilization of SAGRAPE by generating qubit-selective π pulses and employing them to perform noise spectroscopy. For this purpose, we consider the three ^{19}F spins of 1-bromo-2,4,5-trifluorobenzene (BTFBz) that is partially oriented in the liquid crystal *N*-(4-methoxybenzylidene)-4-butylaniline. The molecular structure, resonance offsets $\Omega_k/(2\pi)$, and indirect spin-spin coupling constants J_{kl} of the ^{19}F spins are shown in Fig. 6(a). We applied spin-decoupling to remove the effects of the two hydrogen spins. The noise spectroscopy experiments were carried out in a Bruker 500-MHz NMR spectrometer at an ambient temperature of 300 K.

Noise spectroscopy allows us to characterize the noise spectral density function $S(\nu)$ [33–35] as a function of the noise frequency ν_δ. The experiment involves measuring the decay time-constant $T_2(\delta)$ of the transverse magnetization with a set of CPMG sequences each with a specific inter-π-pulse delay δ, which allows us to sample the noise spectrum

$$S(2\pi\nu_\delta) \sim \frac{\pi^2}{4T_2(\delta)} \tag{14}$$

at frequencies $\nu_\delta = 1/(2\delta)$ [33]. Understanding noise spectra is helpful to develop methods that protect quantum coherence against environmental noise [36]. Carrying out the local noise spectroscopy for each ^{19}F spin needs a set of CPMG sequences involving spin-selective π pulses. Since a train of such π pulses is used for finding the noise amplitude at each noise frequency, the cumulative pulse errors need to be small, thus necessitating the construction of high-fidelity π pulses.

Using SAGRAPE-20 ($\kappa = 20$), we generated three spin-selective π pulses, one for each of the three ^{19}F spins. Each sequence was of the total duration of 360 μs discretized into 360 equal-time segments and had an average fidelity over 0.99 for the RFI parameters $r_m = [0.8, 1, 1.2]$ and $p_m = [0.2, 0.6, 0.2]$, respectively. Using the pulses thus obtained, we performed the experimental local noise spectroscopy on each of the three ^{19}F spins of BTFBz, and the results are shown in Fig. 6(b). These noise spectra are not only helpful in understanding the environment surrounding the spins but also in generating noise-resilient quantum controls tailored for them [36,37]. For the short-pulses discussed here, we may ignore the pulse errors occurring due to external noises. However, for a long control sequence, errors gradually accumulate. In the following section, we describe a general method to train the control algorithm against the external noises.

III. THE ROBUST SAGRAPE (RSAGRAPE)

We now describe generating a control sequence that is robust against the dephasing noise, which generally is the predominant process limiting the coherence time of quantum systems. To train the optimization algorithm against dephasing noise, we introduce an additional term in the Hamiltonian of Eq. (3):

$$H^m(j) = H_0 + H^m_{\rm RF}(j) + H^m_{\rm noise}(j),$$
$$\text{where} \quad H^m_{\rm noise}(j) = 2\pi\eta^m(j)H_z. \tag{15}$$

Here $\eta^m(j) \in [-\zeta/2, \zeta/2]$ is chosen from a uniform random distribution of range ζ. Optimizing in the presence of such a random phase noise renders the control sequence robust against the dephasing effects of the environment. We incorporate this technique of making robust controls with the SAGRAPE algorithm explained in Sec. II to create the RSAGRAPE (robust SAGRAPE) algorithm. Additionally, we can introduce other decoherence-suppression methods such as dynamical decoupling. Here we integrate CPMG pulses within the control sequence as explained below.

We demonstrate the state controllability of RSAGRAPE by preparing controls $\{\omega_\alpha(j)\}$ for two ^{1}H nuclear spins of 2,3,6-trichlorophenol (TCP) dissolved in dimethyl sulphoxide-D6.

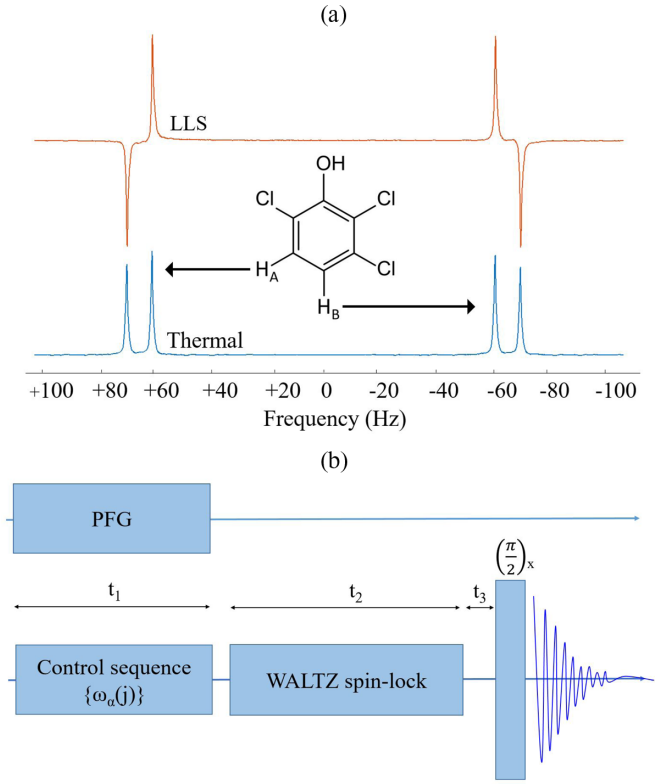

FIG. 7. (a) Molecular structure of TCP, its reference spectrum (labeled thermal), and its LLS spectrum. (b) The NMR pulse sequence for preparing, storing, and detecting the singlet order. A pulsed-field-gradient (PFG) with amplitude randomly varying with time is used to induce phase noise.

The molecular structure and the ^{1}H reference spectrum (in blue) are shown in Fig. 7(a) with the two protons labeled as H_A and H_B. For this system, the difference in the resonance offsets $|\Omega_1 - \Omega_2|/(2\pi)$ is 127.4 Hz and the indirect spin-spin coupling constant J_{12} is 8.8 Hz. The spin-lattice relaxation time constants (T_1) obtained from the inversion recovery experiment were 5.5 and 5.6 s for the spins H_A and H_B, respectively [38].

Our objective is to generate a control sequence $\{\omega_\alpha(j)\}$ that transforms the state of the spin system from thermal equilibrium to the pseudo-singlet-triplet order [see Eq. (12)], which relaxes to the long-lived singlet state (LLS) $-\mathbf{I}_1 \cdot \mathbf{I}_2$ up to an identity representing the background population [39]. While most nonequilibrium quantum states decay to thermal states with a spin-lattice relaxation time constant T_1, the long-lived spin states can retain their spin-order for durations much longer than T_1 [39]. Buoyed by a number of interesting applications in several fields including spectroscopy, medical imaging, and quantum information [40], LLS has recently gained significant attention [41]. Typically, it takes a sequence longer than $1/(2J)$ to prepare the LLS, during which time the noise can cause significant effects.

We prepared the following three control sequences: (i) GRAPE, (ii) GRAPE with CPMG, and (iii) RSAGRAPE-ζ with CPMG. Both (ii) and (iii) are integrated with six CPMG pulses. The robust sequence RSAGRAPE-5 is generated using the RSAGRAPE algorithm with the noise parameter $\zeta = 5$ Hz

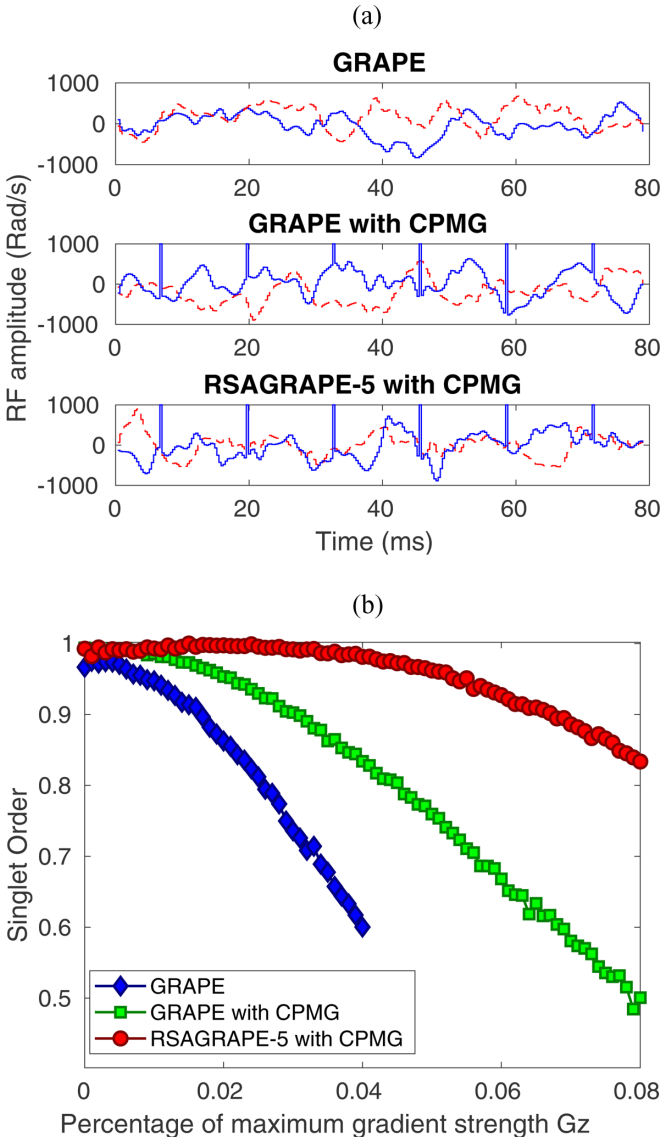

FIG. 8. (a) The RF components $\omega_x(j)$ (blue solid lines, in rad/s) and $\omega_y(j)$ (red dashed lines, in rad/s) corresponding to the three control sequences obtained with GRAPE, GRAPE with CPMG, and RSAGRAPE-5 with CPMG plotted versus time. The latter two sequences are integrated with six CPMG π pulses, each of amplitude $+9941$ rad/s, but their corresponding plots are cropped at ± 1000 rad/s for the visibility purpose. (b) The experimentally observed singlet order versus the maximum gradient strength G_z (in %) for the three control sequences shown in panel (a).

and the SA iteration $\kappa = 10$. Each sequence is of duration $t_1 = 79$ ms, uniformly discretized into 250 segments, and had an average fidelity over 0.99 with the same RFI parameters $r_m = [0.9, 1.0, 1.1]$ and $p_m = [0.2, 0.6, 0.2]$. The three sequences are plotted in Fig. 8(a).

The robustness of the three sequences is tested experimentally again in the Bruker 500-MHz spectrometer at an ambient temperature of 300 K. The NMR pulse sequence for preparing, storing, and measuring the singlet order is shown in Fig. 7(b). After preparing the LLS using each of the control sequences of duration t_1, we stored the LLS under a WALTZ-

16 spin-lock of 2 kHz in amplitude for duration t_2. Finally, we converted the LLS into observable single-quantum magnetization with a free-evolution duration of $t_3 = 1/(4J)$ followed by a $(\pi/2)_x$ pulse. The resulting LLS spectrum consists of a characteristic down-up–up-down spectrum as shown in the top trace of Fig. 7(a). By varying the storage duration t_2, we estimated the lifetime of the singlet order to be 25 s, which is more than four times the T_1 values of the two ^{1}H spins, thus confirming the preparation of the LLS state.

We now experimentally compare the robustness of the three sequences against the dephasing noise. To systematically control the dephasing noise, we introduced a pulsed-field gradient (PFG) G_z that applies a spatial inhomogeneity along the direction of the Zeeman field, i.e., z axis [see Fig. 7(b)]. The amplitude of the PFG was randomly varied over time within a range $[-G_z,\ G_z]$ in each experiment. In subsequent experiments, the amplitude G_z was systematically increased from 0 to 0.08%, where 100% refers to 50 G/cm. In the solution state, the nuclear spins are subjected to controlled decoherence under the combined effects of random PFG and the random molecular motion due to translational diffusion. Finally, we monitored the singlet order by measuring the absolute area of the singlet spectrum obtained after a storage time of $t_2 = 10$ s. The experimental results are shown in Fig. 8(b). Here all the data are normalized with respect to a common datum corresponding to the highest singlet order. It is clear that the simple GRAPE sequence (blue diamond) decays rapidly with the dephasing noise. The singlet order of the GRAPE sequence is lowest even at $G_z = 0$, indicating that it is affected by the intrinsic noise of the spin system and the NMR setup. On the other hand, the GRAPE sequence integrated with CPMG pulses (green square) performs relatively better. In fact, it has the highest singlet order in the absence of external dephasing, i.e., $G_z = 0$. Of course, CPMG only suppresses the dephasing noise up to a cutoff frequency equal to the inverse of the inter-π-pulse delay. Nevertheless, it is evident that RSAGRAPE-5 with CPMG (red circle) is the most robust sequence, which generates high singlet order for a wide range of dephasing noise. Thus, it clearly establishes the superiority of the robust state control sequence generated by the RSAGRAPE algorithm in combating the dephasing noise.

IV. SUMMARY AND OUTLOOK

Quantum control, which is crucial for realizing quantum technologies, is limited by two key factors: (i) convergence efficiency of the optimization algorithms, and (ii) the robustness of the control sequence against external noises. In this work, we address both of these factors.

First, we combined simulated annealing (SA) with the commonly used gradient ascent algorithm (GRAPE) to realize a hybrid algorithm (SAGRAPE). Our numerical analysis confirmed that the convergence efficiency of the SAGRAPE algorithm is significantly improved over the GRAPE algorithm. As a demonstration of an experimental application, we used the SAGRAPE algorithm to generate spin-selective π pulses for three spins in a homonuclear NMR system and obtained their local noise spectra.

Second, we proposed a general method to obtain noise-resilient quantum operations by optimizing the control sequences in the presence of a noisy field. In particular, we designed the RSAGRAPE (robust SAGRAPE) algorithm which generates robust control sequences against dephasing noise. Additionally, we incorporated CPMG pulses along with the control sequence which enhanced their robustness against the external noise. By experimentally comparing the preparation efficiency of long-lived singlet states in the presence of controlled external noise, we confirmed the superiority of the RSAGRAPE sequence over the GRAPE sequences.

Even though this work used the NMR implementation to demonstrate the efficacy of SAGRAPE pulses, the hybrid algorithm can be employed in other architectures such as nitrogen-vacancy centers, superconducting qubits, cold atoms, etc. The concept of incorporating SA can be generalized to other gradient or nongradient algorithms. The computational efficiency of SAGRAPE can be further enhanced by incorporating advanced numerical techniques such as machine learning [42]. The convergence efficiency of the hybrid algorithm may also be further improved by incorporating more advanced variants of simulated annealing such as adaptive simulated annealing [43]. We believe that such hybrid algorithms will play an important role in the future as we attempt to control larger quantum systems with higher precision.

ACKNOWLEDGMENTS

The authors gratefully acknowledge NMR hardware assistance from Nitin Dalvi and Dr. Sandeep Mishra. P.B. acknowledges support from the Prime Minister Research Fellowship. T.S.M. acknowledges funding from DST-QUEST under Grant No. DST/ICPS/QuST/2019/Q67.

[1] E. M. Fortunato, M. A. Pravia, N. Boulant, G. Teklemariam, T. F. Havel, and D. G. Cory, J. Chem. Phys. **116**, 7599 (2002).
[2] T. S. Mahesh and D. Suter, Phys. Rev. A **74**, 062312 (2006).
[3] N. Khaneja, T. Reiss, C. Kehlet, T. Schulte-Herbrüggen, and S. J. Glaser, J. Magn. Reson. **172**, 296 (2005).
[4] P. de Fouquieres, S. Schirmer, S. Glaser, and I. Kuprov, J. Magn. Reson. **212**, 412 (2011).
[5] S. Machnes, E. Assémat, D. Tannor, and F. K. Wilhelm, Phys. Rev. Lett. **120**, 150401 (2018).
[6] T. Caneva, T. Calarco, and S. Montangero, Phys. Rev. A **84**, 022326 (2011).
[7] J. J. W. H. Sørensen, M. O. Aranburu, T. Heinzel, and J. F. Sherson, Phys. Rev. A **98**, 022119 (2018).
[8] N. Khaneja, T. Reiss, B. Luy, and S. J. Glaser, J. Magn. Reson. **162**, 311 (2003).
[9] V. Krotov, Doklady Math. **78**, 949 (2008).
[10] I. I. Maximov, Z. Tošner, and N. C. Nielsen, J. Chem. Phys. **128**, 184505 (2008).

[11] D. M. Reich, M. Ndong, and C. P. Koch, J. Chem. Phys. **136**, 104103 (2012).
[12] R. Eitan, M. Mundt, and D. J. Tannor, Phys. Rev. A **83**, 053426 (2011).
[13] E. Zahedinejad, S. Schirmer, and B. C. Sanders, Phys. Rev. A **90**, 032310 (2014).
[14] G. Bhole, V. S. Anjusha, and T. S. Mahesh, Phys. Rev. A **93**, 042339 (2016).
[15] M. Y. Niu, S. Boixo, V. N. Smelyanskiy, and H. Neven, npj Quantum Inf. **5**, 33 (2019).
[16] Z. An and D. Zhou, Europhys. Lett. **126**, 60002 (2019).
[17] C. A. Ryan, C. Negrevergne, M. Laforest, E. Knill, and R. Laflamme, Phys. Rev. A **78**, 012328 (2008).
[18] C. Negrevergne, T. Mahesh, C. A. Ryan, M. Ditty, F. Cyr-Racine, W. Power, N. Boulant, T. Havel, D. Cory, and R. Laflamme, Phys. Rev. Lett. **96**, 170501 (2006).
[19] L. M. Vandersypen and I. L. Chuang, Rev. Mod. Phys. **76**, 1037 (2005).
[20] Q. Sun, I. Pelczer, G. Riviello, R.-B. Wu, and H. Rabitz, Phys. Rev. A **89**, 033413 (2014).
[21] D. A. Golter, T. Oo, M. Amezcua, K. A. Stewart, and H. Wang, Phys. Rev. Lett. **116**, 143602 (2016).
[22] D. Dong, C. Wu, C. Chen, B. Qi, I. R. Petersen, and F. Nori, Sci. Rep. **6**, 36090 (2016).
[23] J. J. García-Ripoll, P. Zoller, and J. I. Cirac, Phys. Rev. Lett. **91**, 157901 (2003).
[24] M. Grinolds, P. Maletinsky, S. Hong, M. Lukin, R. Walsworth, and A. Yacoby, Nat. Phys. **7**, 687 (2011).
[25] S. Chu, Nature (London) **416**, 206 (2002).
[26] D. G. Cory, R. Laflamme, E. Knill, L. Viola, T. Havel, N. Boulant, G. Boutis, E. Fortunato, S. Lloyd, R. Martinez *et al.*, Fortschr. Phys. **48**, 875 (2000).
[27] D. Suter and T. Mahesh, J. Chem. Phys. **128**, 052206 (2008).
[28] V. Černý, J. Optim. Theory Appl. **45**, 41 (1985).
[29] K. F. C. Yiu, Y. Liu, and K. L. Teo, J. Global Optim. **28**, 229 (2004).
[30] H. Y. Carr and E. M. Purcell, Phys. Rev. **94**, 630 (1954).
[31] S. Meiboom and D. Gill, Rev. Sci. Instrum. **29**, 688 (1958).
[32] G. Dueck and T. Scheuer, J. Comput. Phys. **90**, 161 (1990).
[33] T. Yuge, S. Sasaki, and Y. Hirayama, Phys. Rev. Lett. **107**, 170504 (2011).
[34] G. A. Álvarez and D. Suter, Phys. Rev. Lett. **107**, 230501 (2011).
[35] D. Khurana, G. Unnikrishnan, and T. S. Mahesh, Phys. Rev. A **94**, 062334 (2016).
[36] M. Biercuk, A. Doherty, and H. Uys, J. Phys. B: At., Mol. Opt. Phys. **44**, 154002 (2011).
[37] D. Khurana, B. K. Agarwalla, and T. S. Mahesh, Phys. Rev. A **99**, 022107 (2019).
[38] P. Batra, V. R. Krithika, and T. S. Mahesh, Phys. Rev. Research **2**, 013314 (2020).
[39] M. Carravetta, O. G. Johannessen, and M. H. Levitt, Phys. Rev. Lett. **92**, 153003 (2004).
[40] S. S. Roy and T. S. Mahesh, Phys. Rev. A **82**, 052302 (2010).
[41] G. Pileio, *Long-Lived Nuclear Spin Order: Theory and Applications*, New Developments in NMR Vol. 22 (Royal Society of Chemistry, Cambridge, England, 2020).
[42] P. Batra, M. H. Ram, and T. Mahesh, arXiv:2201.12550 (2022).
[43] L. Ingber, Math. Comput. Modell. **18**, 29 (1993).